RSC Advances

PAPER

View Article Online
View Journal | View Issue

Cite this: *RSC Adv.*, 2017, **7**, 24698

Facile preparation of *in situ* coated $Ti_3C_2T_x$/$Ni_{0.5}Zn_{0.5}Fe_2O_4$ composites and their electromagnetic performance

Youbing Li,[ab] Xiaobing Zhou,[*bc] Jing Wang,[a] Qihuang Deng,[b] Mian Li,[b] Shiyu Du,[b] Young-Hwan Han,[c] Jaehyung Lee[*c] and Qing Huang[*b]

Received 23rd March 2017
Accepted 30th April 2017

DOI: 10.1039/c7ra03402d

rsc.li/rsc-advances

A novel family of $Ti_3C_2T_x$/ferrite composites with high reflection loss was developed using a facile *in situ* co-precipitation method. The as-synthesized $Ti_3C_2T_x$/ferrite composite with a 5 wt% $Ti_3C_2T_x$ MXenes loading exhibited high reflection loss (−42.5 dB) at 13.5 GHz. The effective absorption bandwidth of the 5 wt% $Ti_3C_2T_x$/$Ni_{0.5}Zn_{0.5}Fe_2O_4$ composite reached ~3 GHz (12–15 GHz) in the K-band. The incorporation of $Ti_3C_2T_x$ MXenes improved the electromagnetic impedance of the $Ti_3C_2T_x$/$Ni_{0.5}Zn_{0.5}Fe_2O_4$ composite resulting from the enhanced electrical conductivity. The potential electromagnetic wave absorption mechanisms were revealed, which may contain magnetic loss, dielectric loss, conductivity loss, multiple reflections, and scattering. The technique is facile, fast, scalable, and favorable for the commercialization of this composite. This study provides a potential way to develop EM wave absorbing materials for a large family of MXenes/ferrite composites.

1. Introduction

Electromagnetic (EM) radiation pollution is attracting increasing attention because it affects human health and the operation of electronic devices. High-performance electromagnetic interference (EMI) absorbing and shielding materials have attracted growing interest as a way to solve these problems.[1–3] Three typical mechanisms are involved in the design of promising EMI absorbing and shielding materials suggested by Shahzad *et al.*[4] The first is to interact with the EM fields by charge carries, which require materials with high electrical conductivity. The secondary mechanism is absorbing EM radiation by the materials electric and/or magnetic dipoles interacting with radiation. The third mechanism is accounting for multiple internal reflections that arise from scattering centers and interfaces or defect sites within the shielding material, resulting in scattering and the absorption of EM waves. Therefore, a hybrid material that combines high electrical conductivity, magnetic loss, and multiple reflections was reported to be a promising candidate for EMI absorbing and shielding.[5] Furthermore, the effective absorption of composites was usually defined as reflection loss (RL) <−10 dB, which corresponds to more than 90% EM wave energy absorbed. The corresponding frequency range (RL < −10 dB) is denoted as the effective absorption bandwidth. The reflection loss (RL) values of the composites can be calculated using the transmission line theory:[6,7]

$$\mathrm{RL}\ (\mathrm{dB}) = 20 \log \left| \frac{Z_{\mathrm{in}} - 1}{Z_{\mathrm{in}} + 1} \right| \quad (1)$$

$$Z_{\mathrm{in}} = \sqrt{\frac{\mu_{\mathrm{r}}}{\varepsilon_{\mathrm{r}}}} \tanh \left[j \frac{2\pi f d}{c} \sqrt{\mu_{\mathrm{r}} \varepsilon_{\mathrm{r}}} \right] \quad (2)$$

where Z_{in} is the input impedance of the absorbing materials at the input interface, μ_{r} and ε_{r} are the complex magnetic permeability and the complex permittivity respectively, f is the frequency, d is the thickness of the absorber, and c is the light velocity in a vacuum. Therefore, from eqn (1) and (2), RL is decided by Z_{in} which is determined by the μ_{r} and ε_{r} of the materials. Thus the impedance matching is very important for hybrid EM absorbers.

Ni–Zn ferrites have been considered promising candidates as EM absorbers owing to their appropriate permeability and permittivity.[5,8,9] On the other hand, Ni–Zn ferrites attenuate the EM wave mainly through magnetic loss and lead to the impedance matching is out of balance.[10] Furthermore, the high resistivity and narrow absorption bandwidth have limited their applications as EMI absorbers.[11–13] To solve these problems, high electrical conducting one-dimensional (1D) carbon nanotubes (CNTs) and two-dimensional (2D) graphene were

[a]School of Materials Science and Engineering, Anhui University of Science and Technology, Huainan, Anhui 232001, China

[b]Engineering Laboratory of Specialty Fibers and Nuclear Energy Materials (FiNE), Ningbo Institute of Materials Technology and Engineering, Chinese Academy of Sciences, Ningbo, Zhejiang 315201, China. E-mail: zhouxb@nimte.ac.cn; huangqing@nimte.ac.cn

[c]School of Materials Science and Engineering, Yeungnam University, Gyeongsan, Korea. E-mail: jhlee@ynu.ac.kr

introduced to ferrites.[14–17] In our previous work,[14,15] CNTs were coated *in situ* with $Ni_{0.5}Zn_{0.5}Fe_2O_4$ by a combined precipitation-hydrothermal method. The results showed that when the CNT content was 5 wt%, the reflection ratios were less than −10 dB within the frequency range, 2–9 GHz, and the reflection ratios reached a minimum −32.5 dB at 3.9 GHz. Shen *et al.*[18] developed a novel polyetherimide (PEI)/grapheme@Fe_3O_4 (G@Fe_3O_4) composite foams, and when the G@Fe_3O_4 loading was 10 wt%, the PEI/G@Fe_3O_4 foam exhibited a high EMI shielding effectiveness of ~41.5 dB (g^{-1} cm^{-3}) at 8–12 GHz. They suggested that most of the applied microwave was absorbed rather than reflected, resulting from the improved impedance matching, electromagnetic wave attenuation, and multiple reflections.

MXenes, developed by Naguib *et al.*,[19] are a new family of 2D transition metal carbides and/or nitrides obtained by etching the A layer of MAX phases, where M represents a transition metal, "A" are elements in the group 13–16, "X" represents carbon and/or nitrogen. The exposed transition-metal surfaces are terminated with a mixture groups (T_x), such as –OH, =O, and –F, after HF etching.[20] More than 20 different MXenes have been synthesized.[21] MXenes exhibit promising potential applications as Li-ion batteries and supercapacitors owing to their excellent chemical and physical properties.[22,23] Recently, Han *et al.*[24] developed 2D $Ti_3C_2T_x$ (where T_x denotes the surface terminated groups) MXenes for novel EM absorbing applications. The fundamental EM loss mechanisms of $Ti_3C_2T_x$ before and after annealing were revealed. They suggested that the formation of a localized sandwich structure composed of TiO_2 nanocrystals and amorphous carbon without sacrificing the original 2D layer structure improved the microwave absorbing capability. Moreover, Shahzad *et al.*[4] first developed highly flexible MXene films and nacre-like MXene-sodium alginate (SA) composite films for EMI shielding. They reported that a 45 μm thick $Ti_3C_2T_x$ film exhibited an EMI shielding effectiveness of 92 dB (>50 dB for a 2.5 mm film), which is the highest among synthetic materials of comparable thickness produced to date. The excellent electrical conductivity of $Ti_3C_2T_x$ films (4600 S cm^{-1}) and multiple internal reflections from $Ti_3C_2T_x$ flakes in free-standing films were considered the reason for the high EMI shielding effectiveness. Furthermore, they suggested that the surface terminated groups (–OH, =O, and –F,) play a role on the high EMI shielding effectiveness. The ability of each element to interact with input electromagnetic waves leads to polarization losses, which in turn improve the overall shielding.

Therefore, $Ti_3C_2T_x$ MXenes are promising candidates as EMI absorbing materials.[4,24,25] Moreover, $Ti_3C_2T_x$ terminated with negative groups (–OH, and –F) can be potentially coated with metal positive ions (such as Ni^{2+}, Zn^{2+}, and Fe^{2+}). Herein, a novel $Ti_3C_2T_x/Ni_{0.5}Zn_{0.5}Fe_2O_4$ composite, which potentially combines three EM wave absorbing mechanisms, was designed and synthesized. A facile chemical co-precipitation approach was developed to ensure that the $Ti_3C_2T_x$ flakes were coated *in situ* with $Ni_{0.5}Zn_{0.5}Fe_2O_4$ ferrites, and without oxidation and sacrificing the original layer structure. The phase, microstructure, and electromagnetic properties of $Ti_3C_2T_x/Ni_{0.5}Zn_{0.5}Fe_2O_4$ composites were investigated systematically. To the best of the authors' knowledge, this is the first effort to reveal the EM loss mechanisms of $Ti_3C_2T_x/Ni_{0.5}Zn_{0.5}Fe_2O_4$ composites. The combination of $Ti_3C_2T_x$ MXenes may not only improve the impedance matching characteristics, but also combine the advantages of the individual components. The present work paves the way to develop a large family of MXenes/ferrites composites for EM wave absorbing.

2. Experimental section

2.1 Materials

Elemental powders of TiC (~200 mesh, 99% purity), Ti (~200 mesh, 99% purity), and Al (~300 mesh, 99% purity) were commercially obtained from Target Research Center of General Research Institute for Nonferrous Metals, Beijing, China. Nickel nitrate ($Ni(NO_3)_2 \cdot 6H_2O$), zinc nitrate ($Zn(NO_3)_2 \cdot 6H_2O$), ferric nitrate ($FeSO_4 \cdot 7H_2O$), sodium hydroxide (NaOH), sodium lignosulfonate (SLS), and hydrofluoric acid (HF) were commercially obtained from Aladdin Chemical Reagent, China.

2.2 Preparation and functionalization of $Ti_3C_2T_x$ MXenes

The Ti_3AlC_2 (purity of 98.5 wt%, containing a small amount of TiC and Al_2O_3 impurity phases, 300 mesh) was synthesized by the spark plasma sintering (SPS) of a mixture of Ti, Al, and C in a fixed mole ratio at 1400 °C for 20 min. After cooling to room temperature, the as-prepared Ti_3AlC_2 bulk samples were pulverized to powders and passed through a 300 mesh screen. The $Ti_3C_2T_x$ powders were synthesized using the procedure suggested by Naguib *et al.*[19] A 1 g sample of Ti_3AlC_2 powder was added to a 10 ml of a HF solution (40 wt%) for 72 h at room temperature, the solution was stirred lightly every 12 h. The as-received solution was centrifuged, washed with deionized water and alcohol, and dried at room temperature for 48 h. To improve the dispersion behavior of the $Ti_3C_2T_x$ powders in water. The obtained $Ti_3C_2T_x$ powders were functionalized by a disperser of sodium lignin sulfonate (SLS). Typically, 0.1 g $Ti_3C_2T_x$ powders and 0.05 g SLS were added to 100 ml deionized water, followed by another ultrasonic dispersion process for 45 min. Finally, a modified 1 mg ml^{-1} $Ti_3C_2T_x$ dispersion solution was obtained after removing the excessive SLS by filtration and washing.

2.3 Preparation of *in situ* coated $Ti_3C_2T_x/Ni_{0.5}Zn_{0.5}Fe_2O_4$ composites

The desired amount of the $Ti_3C_2T_x$ dispersion solution was added to a salt solution composed of $Ni(NO_3)_2 \cdot 6H_2O$, $Zn(NO_3)_2 \cdot 6H_2O$, and $FeSO_4 \cdot 7H_2O$ at a molar ratio of Ni : Zn : Fe = 0.5 : 0.5 : 2 according to the stoichiometric ratio of $Ni_{0.5}Zn_{0.5}Fe_2O_4$, followed by magnetic stirring and ultrasonic dispersing for 60 min. According to the thermodynamic calculations reported in the literature, the pH needs to be controlled at 10.5 to fabricate the expected ferrite.[26] The salt and $Ti_3C_2T_x$ of the mixed solution and 1 M NaOH solution were added dropwise at a flow rate of 2.5 ml min^{-1} under continuous stirring with O_2 pumped into the reaction solution. After co-precipitation, a Ni, Zn, and Fe precursor slurry formed and

then continued to react at 80 °C for 4 h. The finally obtained precipitates were washed 5 times with deionized water and absolute ethanol, dried, ground, and passed through a 200 mesh sieve; the final $Ti_3C_2T_x/Ni_{0.5}Zn_{0.5}Fe_2O_4$ composites were obtained. The schematic presents the facile co-precipitation processing of the $Ti_3C_2/Ni_{0.5}Zn_{0.5}Fe_2O_4$ composites (Fig. 1).

2.4 Characterization

X-ray diffraction (XRD, D8 Advance, Bruker AXS, Germany) was used to analyze the sample phase; the XRD data were collected using Cu Kα radiation at a step size of 0.02°/2θ with a collection time of 1 s per step. Fourier transform infrared (FTIR, Thermo, Nicolet6700, USA) spectroscopy was used to characterize the functional groups on the surface before and after the functionalization of $Ti_3C_2T_x$. The microstructure and chemical composition were observed by scanning electron microscopy (SEM, QUANTA 250 FEG, FEI, USA) equipped with an energy dispersive spectroscopy (EDS) system. Transmission electron microscopy (TEM Tecnai F20, FEI, USA) and high-resolution TEM (HRTEM) images were carried out at an acceleration voltage of 200 kV. The specific surface area was measured using the Brunauer–Emmett–Teller (BET)[27] method on an ASAP2020 instrument. The electromagnetic property was measured using a physical properties measurement system (PPMS, Quantum Design, USA) at the room temperature hysteresis loop.

The permittivity and permeability were measured using a microwave vector network analyser (8722ES, Agilent, USA) in the frequency range of 0.2–18 GHz. The specimens used for the permittivity and permeability property measurements were fabricated by mixing different $Ti_3C_2T_x$ contents of the $Ti_3C_2T_x/Ni_{0.5}Zn_{0.5}Fe_2O_4$ composites with 20 wt% paraffin. Typically, the composites and paraffin were dispersed in hexane after grinding to avoid aggregation. The mass ratio of paraffin to composite powders is 1 : 4. After the solvent was volatilized, the mixed powders were cold-pressed into the samples with a toroid (outside diameter is 7 mm, inside diameter is 3 mm, and thickness of 2 mm) under a pressure of 5 MPa. After that, the specimens were inserted into a copper holder and connected between the waveguide flanges of the instrument. The complex permittivity and permeability of the samples were calculated from S parameters (S_{11} and S_{21}) which measured from vector network analyzer using the coaxial-line transmission method.

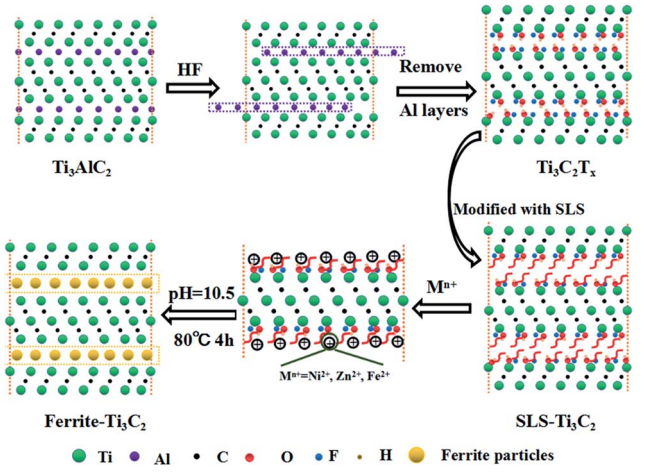

Fig. 1 Schematic diagram of the co-precipitation processing of $Ti_3C_2T_x/Ni_{0.5}Zn_{0.5}Fe_2O_4$ composites.

3. Results and discussion

Fig. 2a presents XRD patterns of the as-received Ti_3AlC_2 powders and after HF etching $Ti_3C_2T_x$ MXenes. The Ti_3AlC_2 typical XRD peak of (104) at 39° 2θ disappeared and was replaced with a low intensity broadened peak. This indicates that the Al atomic layers had been exfoliated successfully and the corresponding 2D $Ti_3C_2T_x$ MXenes had formed after HF etching. At the same time, new XRD peaks for $Ti_3C_2F_2$ were detected at 8.9° and 18.4° 2θ showing that F was inserted into the $Ti_3C_2T_x$ MXenes interlayer.[28] Furthermore, a new peak at 27.4° 2θ was detected, which was assigned to $Ti_3C_2(OH)_2$.[28] These results suggest that the $Ti_3C_2T_x$ surfaces were terminated with functional groups of –OH, and –F after HF etching. Fig. 1b and c exhibit SEM images of Ti_3AlC_2 and as-obtained $Ti_3C_2T_x$ MXenes after HF etching, respectively. Ti_3AlC_2 exhibited a typical layered structure, as shown in Fig. 2b. After HF etching, a similar accordions' 2D layered structure was formed by extracting an Al atom from Ti_3AlC_2 (Fig. 2c). The terminated negative groups of –OH, and –F combined with the 2D layered structure provides potential channels for Ni, Zn, and Fe ion intercalation. Fig. 2d shows a TEM image of the $Ti_3C_2T_x$ MXenes sheets. The material showed a similar hexagonal symmetry and crystallinity to that of the parent Ti_3AlC_2 phase, as indicated by the fast Fourier transform (FFT) pattern shown in the inset image in Fig. 2d.

The uniform distribution of $Ti_3C_2T_x$ MXenes in the matrix of ferrite is a critical issue for $Ti_3C_2T_x/Ni_{0.5}Zn_{0.5}Fe_2O_4$ composites. Although $Ti_3C_2T_x$ MXenes has good hydrophilicity for the terminated surface groups of –OH, =O, and –F. To further improve the dispersion behavior of $Ti_3C_2T_x$ MXenes in water and provide a convenient path for Ni^{2+}, Zn^{2+}, and Fe^{2+} intercalation, the $Ti_3C_2T_x$ MXenes were modified with amphiphilic sodium lignin sulfonate (SLS) surfactants. Fig. 3 shows the FTIR spectra of $Ti_3C_2T_x$ with and without functionalization by SLS. The existence of hydroxyl groups was confirmed by the absorption peaks at 3437 cm^{-1} and 1636 cm^{-1}, which were assigned to the absorbed external water and strongly hydrogen-bonded OH or extremely strong coordinated H_2O in the two samples.[29] In addition, the peak at 620 cm^{-1} was probably due to the deformation vibration of the Ti–O bond;[30] the C–F (1097 cm^{-1}) and O–H (1399 cm^{-1}) groups were observed in the spectra of the two samples.[31] The $-CH_2$ (2920 cm^{-1}), –C=C– (1560 cm^{-1}), aromatic ring (1508 cm^{-1}), C–H (1458 cm^{-1}) group, and C–O (1120 cm^{-1}) were present in the spectra of SLS–Ti_3C_2.[14,32] Lignin sulfonic is an amphoteric hydrophilic polymer surfactant with both carbon chains, phenolic hydroxyl hydrophobic group and hydrophilic group of sulfonic acid. Under the effect of van der Waals forces and steric hindrance effects, the hydrophobic group improved the dispersion of $Ti_3C_2T_x$ MXenes in water, and the hydrophilic group stretched in the aqueous

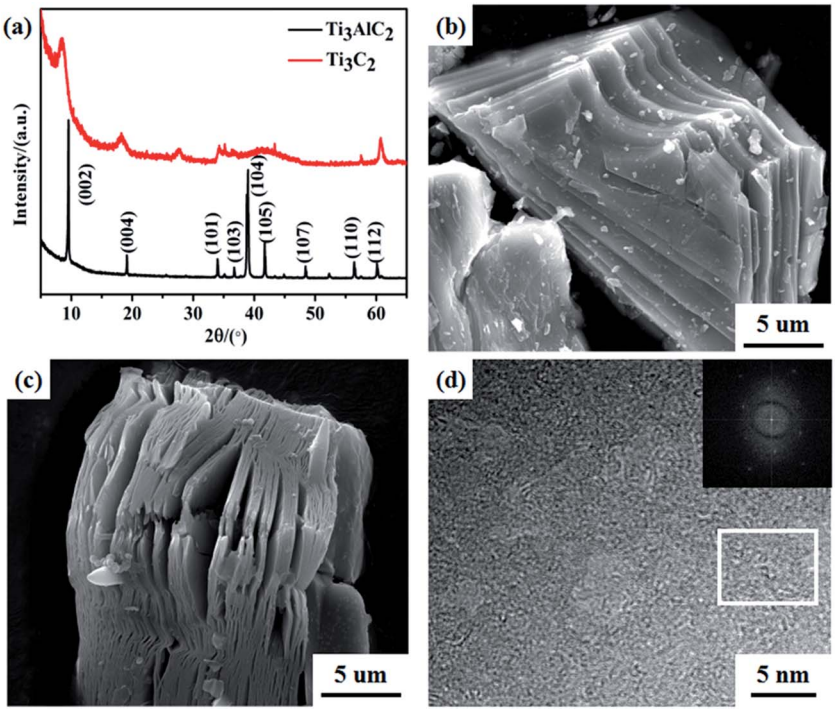

Fig. 2 (a) XRD patterns of Ti_3AlC_2 and $Ti_3C_2T_x$ MXenes. SEM images of Ti_3AlC_2 (b) and $Ti_3C_2T_x$ (c). (d) HRTEM image of $Ti_3C_2T_x$ sheets, the inset shows the FFT of the white rectangle area.

solution and provided a nucleation channel for the *in situ* coated and intercalated NiZn ferrite.

The dispersion behavior of $Ti_3C_2T_x$ MXenes after modification by SLS was examined. Fig. 4 shows the zeta potential of $Ti_3C_2T_x$ MXenes after surface functionalization in the pH range of 4–11. The pH was tuned by diluted sodium hydroxide and nitric acid. Over the entire pH range, the zeta potential decreased with increasing pH (slight fluctuations were observed at pH = 9 and 11 for the measurement error). The zeta potential in the entire measured pH range was lower than −25 mV, which is the standard surface potential value of a stable dispersion colloidal solution. The zeta potential reached approximately −40 mV at the Ni^{2+}, Zn^{2+}, and Fe^{2+} co-precipitation pH of 10.5 ± 0.1.[15] Therefore, after functionalization by SLS, a large number of negative charges were modified on the surface of $Ti_3C_2T_x$ MXenes. The aggregation of $Ti_3C_2T_x$ MXenes can be prevented by coulomb repulsion and steric-hindrance. On the other hand, the large number of negative charges would absorb Ni^{2+}, Zn^{2+}, and Fe^{2+}, which is a benefit to the NiZn ferrite *in situ* coated $Ti_3C_2T_x$ MXenes surface and intercalated into the $Ti_3C_2T_x$ MXenes interlayer. Furthermore, the local dipole polarization may be induced between the surface functional groups and Ti_3C_2 when subjected to an alternating EM field.[4]

The chemical co-precipitation process is a facile scale approach to the synthesis of NiZn ferrite. After modification by SLS, $Ti_3C_2T_x$ were mixed with the salt solution of $Ni(NO_3)_2 \cdot 6H_2O$, $Zn(NO_3)_2 \cdot 6H_2O$, and $FeSO_4 \cdot 7H_2O$. $Ti_3C_2T_x/Ni_{0.5}Zn_{0.5}Fe_2O_4$ composites with different $Ti_3C_2T_x$ contents were synthesized by a co-precipitation process at 80 °C for 4 h. Fig. 5 presents the XRD patterns of pure $Ni_{0.5}Zn_{0.5}Fe_2O_4$ and $Ti_3C_2T_x/Ni_{0.5}Zn_{0.5}Fe_2O_4$ composites with different $Ti_3C_2T_x$ contents. All

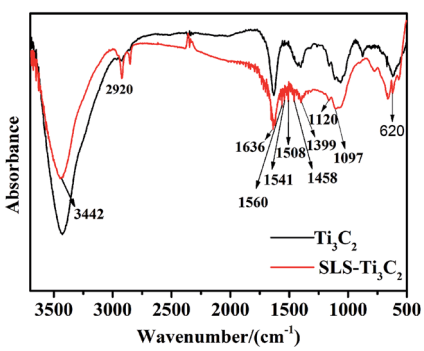

Fig. 3 FTIR spectra of $Ti_3C_2T_x$ MXenes with and without functionalization.

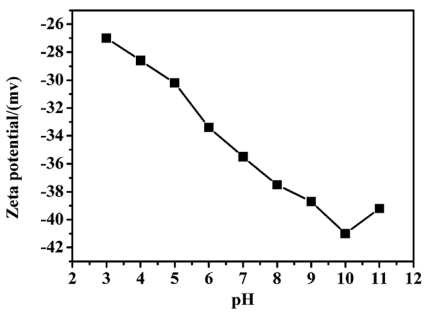

Fig. 4 Zeta potential as a function of pH for the surface functionalization of $Ti_3C_2T_x$ MXenes.

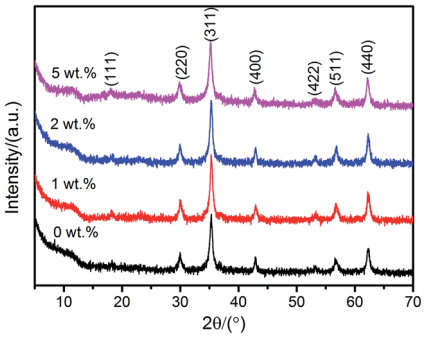

Fig. 5 XRD patterns of pure $Ni_{0.5}Zn_{0.5}Fe_2O_4$ and $Ti_3C_2T_x/Ni_{0.5}Zn_{0.5}Fe_2O_4$ composites with various $Ti_3C_2T_x$ contents synthesized at 80 °C for 4 h.

the specimens showed a typical spinel phase and good crystallization. The characteristic XRD peaks at 18.05°, 30.02°, 35.29°, 43.01°, 53.28°, 56.80° and 62.27° 2θ correspond to the (111), (220), (311), (400), (422), (511) and (440) plane of $Ni_{0.5}Zn_{0.5}Fe_2O_4$ crystal, respectively. This is consistent with the Joint Committee on Powder Diffraction Standards (JCPDS) card no. 8-234. The typical XRD peaks of $Ti_3C_2T_x$ MXenes at 8.9° and 18.4° 2θ were not detected, which may due to the low content of $Ti_3C_2T_x$ MXenes, and/or full coverage of $Ni_{0.5}Zn_{0.5}Fe_2O_4$ nanocrystals on the $Ti_3C_2T_x$ surface. Moreover, no anatase or rutile phases were detected, which indicates that $Ti_3C_2T_x$ MXenes was not oxidized due to the facile low temperature co-precipitation process. The mean grain sizes of the $Ti_3C_2T_x/Ni_{0.5}Zn_{0.5}Fe_2O_4$ composites with different $Ti_3C_2T_x$ contents were calculated from the XRD patterns using Scherrer's equation:[33]

$$D = k\lambda/\beta \cos\theta \quad (3)$$

where D is the mean grain size, k is a constant (0.89), λ is the wavelength of X-rays and equal to 0.154056 nm, β is the half-peak width, and θ is the diffraction angle. The mean grain sizes of pure $Ni_{0.5}Zn_{0.5}Fe_2O_4$ and $Ti_3C_2T_x/Ni_{0.5}Zn_{0.5}Fe_2O_4$ composites with different $Ti_3C_2T_x$ contents were 14.8 nm, 13.5 nm (1 wt%), 12.4 nm (2 wt%), and 10.5 nm (5 wt%), respectively.

Interestingly, the mean grain size of the $Ti_3C_2T_x/Ni_{0.5}Zn_{0.5}Fe_2O_4$ composites decreased with increasing $Ti_3C_2T_x$ content. This can be obtained from the NiZn ferrite formation mechanism of the $Ti_3C_2T_x$ surfaces. There were three steps as follows:[33]

(i) Initially, Ni^{2+}, Zn^{2+}, and Fe^{2+} were absorbed *in situ* by the large number of negative charges of the $Ti_3C_2T_x$ surfaces. They were co-precipitated by adding a NaOH solution. $Fe(OH)_2$ formed first because of the higher Fe^{2+} concentration than Ni^{2+} and Zn^{2+} (eqn (4)). At the same time, the gel of $[Fe(OH)_3]_m$ formed after the oxidation of $Fe(OH)_2$ with pumped O_2 (eqn (5) and (6)).

$$Fe^{2+} + 2OH^- \rightarrow Fe(OH)_2 \quad (4)$$

$$Fe(OH)_2 + \frac{1}{2}O_2 \rightarrow Fe(OH)_3 \quad (5)$$

$$mFe(OH)_3 \rightarrow [Fe(OH)_3]_m \quad (6)$$

(ii) According to the Fajans rule, Ni^{2+} and Zn^{2+} should be absorbed on the surface of colloid cores ($[Fe(OH)_3]_m$) because the colloid cores preference absorbed those metal ions, which can form thawless materials with Fe. When Ni^{2+} and Zn^{2+} were adsorbed on the colloid cores surface, hydrolysis of the metal ions took place, and the hydroxyl resembling the metal ions were then obtained.

$$[Fe(OH)_3]_m + Ni^{2+} + Zn^{2+} + OH^- \rightarrow [Fe(OH)_3]_m \cdot Ni(Zn)OH^+ \quad (7)$$

(iii) In the last stage, as the reaction proceeded, the intermediate was transformed gradually to NiZn ferrite with the release of a proton, which can be written as:

$$[Fe(OH)_3]_m \cdot Ni(Zn)OH^+ \rightarrow NiZnFe_2O_4 + H_2O + H^+ \quad (8)$$

Therefore, the number of negative charges on the surface of $Ti_3C_2T_x$ increased with increasing $Ti_3C_2T_x$ content, which would provide more channels to absorb metal ions and form more colloid cores ($[Fe(OH)_3]_m$). Those larger number of colloid cores ($[Fe(OH)_3]_m$) will improve the nucleation of NiZn ferrite. Grain growth was inhibited compared to the free or lower contents of $Ti_3C_2T_x/Ni_{0.5}Zn_{0.5}Fe_2O_4$ composites. Therefore, the grain size decreased with increasing $Ti_3C_2T_x$ content. On the other hand, the second phase of $Ti_3C_2T_x$ may prevent grain growth, as observed in graphene/ceramic composites.[34] As the contents of $Ti_3C_2T_x$ increased, the collision probabilities between the second phase of $Ti_3C_2T_x$ and metal ions would increase, which might impede NiZn ferrite grain growth.

Furthermore, the grain size can be reflected indirectly by the specific surface areas. The specific surface areas of the pure $Ni_{0.5}Zn_{0.5}Fe_2O_4$, pure $Ti_3C_2T_x$, and $Ti_3C_2T_x/Ni_{0.5}Zn_{0.5}Fe_2O_4$ composites with various $Ti_3C_2T_x$ contents were measured using the BET method. Fig. 6 presents the specific surface areas of the $Ti_3C_2T_x/Ni_{0.5}Zn_{0.5}Fe_2O_4$ composites with various $Ti_3C_2T_x$ contents. The specific surface areas of the pure $Ni_{0.5}Zn_{0.5}Fe_2O_4$ and as-received $Ti_3C_2T_x$ MXenes were 53.17 $m^2\ g^{-1}$ and 13.91 $m^2\ g^{-1}$, respectively. The specific surface areas of the $Ti_3C_2T_x/$

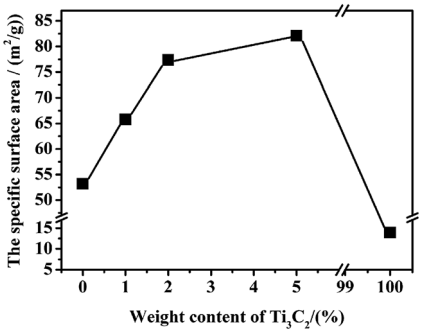

Fig. 6 Specific surface areas of pure $Ni_{0.5}Zn_{0.5}Fe_2O_4$, pure $Ti_3C_2T_x$ MXenes, and $Ti_3C_2T_x/Ni_{0.5}Zn_{0.5}Fe_2O_4$ composites with different $Ti_3C_2T_x$ contents.

$Ni_{0.5}Zn_{0.5}Fe_2O_4$ composites increased with increasing $Ti_3C_2T_x$ MXenes content, and reached a maximum of 82.01 $m^2\ g^{-1}$ for the 5 wt% $Ti_3C_2T_x/Ni_{0.5}Zn_{0.5}Fe_2O_4$ composites. This indicates that finer grain $Ti_3C_2T_x/Ni_{0.5}Zn_{0.5}Fe_2O_4$ composites were obtained at higher $Ti_3C_2T_x$ MXenes contents. This is consistent with the grain size calculation from the XRD patterns. The incorporation of the nonmagnetic phase of $Ti_3C_2T_x$ MXenes impeded the serious aggregation of magnetic NiZn ferrite nanoparticles.

SEM and TEM were carried out to further examine the microstructure of the as-synthesized $Ti_3C_2T_x/Ni_{0.5}Zn_{0.5}Fe_2O_4$ composites. Fig. 7a shows a typical SEM image of the 5 wt% $Ti_3C_2T_x/Ni_{0.5}Zn_{0.5}Fe_2O_4$ composites. $Ti_3C_2T_x$ MXenes were covered homogenously with spherical NiZn ferrite nanoparticles, and $Ti_3C_2T_x$ MXenes still retained the ordered layer structure. NiZn ferrite nanoparticles had a tendency to agglomerate because of the powerful magnetic dipole interactions and high surface energy. EDS was carried out to confirm the chemical composition of the composites. EDS analysis of the rectangle area marked in Fig. 7a revealed mainly Ti, C, O, Ni, Zn, and Fe (Fig. 7b). S and Na were not detected, showing that the SLS surfactant and NaOH precipitant can be removed by filtration and washing with water. Fig. 6c presents the HRTEM image of 5 wt% $Ti_3C_2T_x/Ni_{0.5}Zn_{0.5}Fe_2O_4$ composites. The ferrite nanograins covered not only the surface of the $Ti_3C_2T_x$ MXenes sheets, but were also inserted into the $Ti_3C_2T_x$ MXenes interlayer. The mean grain size of $Ni_{0.5}Zn_{0.5}Fe_2O_4$ was approximately 10 nm, which was very close to the value calculated from the XRD patterns. After detailed analysis of the lattice fringes, the lattice fringe spacing 0.25 nm (Fig. 7c) can be assigned to the (311) planes of the cubic spinel crystal $Ni_{0.5}Zn_{0.5}Fe_2O_4$. The corresponding selected area electron diffraction (SAED) pattern also indicates the good crystal structure of the cubic spinel phase. The lattice fringe spacing 0.48 nm (Fig. 7c) was a typical (0004) plane of the hexagonal structure of $Ti_3C_2T_x$ MXenes. Therefore, the morphology of the 5 wt% $Ti_3C_2T_x/Ni_{0.5}Zn_{0.5}Fe_2O_4$ composites further demonstrated that a large number of modified $Ti_3C_2T_x$ MXenes surface negative charges acted as nucleation centers and interacted with metal ions during co-precipitation, which was a benefit to the *in situ* coating by $Ni_{0.5}Zn_{0.5}Fe_2O_4$ nanoparticles. Furthermore, $Ni_{0.5}Zn_{0.5}Fe_2O_4$ nanoparticles were attached firmly to the surface and were inserted into the interlayer of $Ti_3C_2T_x$ MXenes, and an ultrasonication processing was performed during TEM specimen preparation, which indicated an excellent electrostatic interaction between $Ti_3C_2T_x$ and ferrites.

The magnetic properties of the $Ti_3C_2T_x/Ni_{0.5}Zn_{0.5}Fe_2O_4$ composites with various $Ti_3C_2T_x$ contents were examined in an applied magnetic field range from −30 to 30 kOe at room temperature. Fig. 8 shows the hysteresis loop of the $Ti_3C_2T_x/Ni_{0.5}Zn_{0.5}Fe_2O_4$ composites with different $Ti_3C_2T_x$ contents. All of them exhibited typical soft ferrite properties because the coercive force and residual magnetization are nearly zero. Compared to the pure $Ni_{0.5}Zn_{0.5}Fe_2O_4$, the saturation magnetization (M_s) of the 5 wt% $Ti_3C_2T_x/Ni_{0.5}Zn_{0.5}Fe_2O_4$ composites decreased from 32.3 to 27.08 emu g^{-1}. The M_s decreased slightly with decreasing $Ti_3C_2T_x$ contents. The decrease in M_s might be due to the demagnetizing field produced by the incorporation of nonmagnetic $Ti_3C_2T_x$ and the decreasing grain size. Xia Li *et al.*[33] observed similar trends for pure NiZn ferrite

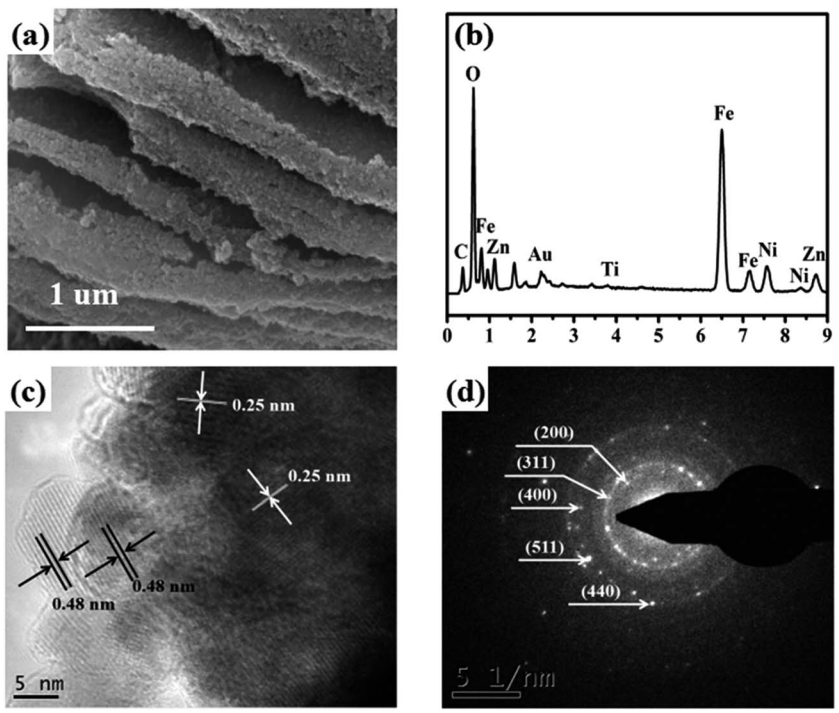

Fig. 7 (a) SEM image of 5 wt% $Ti_3C_2T_x/Ni_{0.5}Zn_{0.5}Fe_2O_4$ composites and EDS (b) spectra of the white area in (a); HRTEM image (c) and SAED pattern (d) of 5 wt% $Ti_3C_2T_x/Ni_{0.5}Zn_{0.5}Fe_2O_4$ composites.

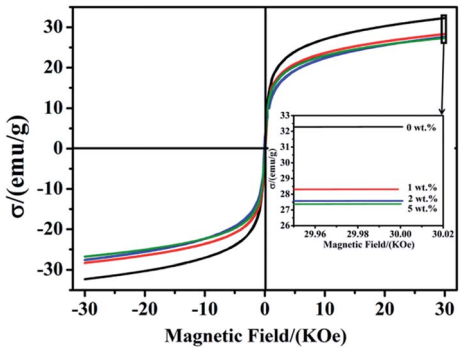

Fig. 8 Hysteresis loops of $Ti_3C_2T_x/Ni_{0.5}Zn_{0.5}Fe_2O_4$ composites with various $Ti_3C_2T_x$ contents: (a) 0 wt%, (b) 1 wt%, (c) 2 wt%, (d) 5 wt%.

nanoparticles. Compared to the 19 nm NiZn nanoparticles, the saturation magnetization of 6 nm NiZn nanoparticles decreased from 38 to 32 emu g^{-1}. Kodama *et al.*[35] attributed this to much more frozen spins on the surface that point to random positions, which reduced the saturation magnetization for finer particles.

To examine the EM wave absorption of the as-synthesized $Ti_3C_2T_x/Ni_{0.5}Zn_{0.5}Fe_2O_4$ composites, their relative complex permittivity and complex permeability were measured in the frequency range of 0.2–18 GHz. The complex permittivity and permeability are usually used to analyze the dielectric and magnetic properties of the microwave absorber materials. Generally, real part of the permittivity and permeability signify the storage capability of the dielectric and magnetic energy, respectively. While the imaginary part of the permittivity and permeability stand for the loss of dielectric and magnetic energy.[36] Fig. 9a–d shows the permittivity and permeability of pure $Ni_{0.5}Zn_{0.5}Fe_2O_4$ and $Ti_3C_2T_x/Ni_{0.5}Zn_{0.5}Fe_2O_4$ composites with various $Ti_3C_2T_x$ contents, respectively. Both the real (ε') and imaginary (ε'') part of the permittivity of the $Ti_3C_2T_x/Ni_{0.5}Zn_{0.5}Fe_2O_4$ composites increased with increasing $Ti_3C_2T_x$ contents (Fig. 9a and b). A high electrical conductivity is benefit to a high complex permittivity according to free electron theory.[37] Therefore, these increases are mainly due to the high electrical conductivity of $Ti_3C_2T_x$, which are already indicated by both the theoretical prediction and experimental results. $Ti_3C_2T_x$ shows the metallic-like electrical conductivity behavior, which was attributed to the high electron density of states near the Fermi level [$N(E_f)$], as simulated from density functional theory.[22] Shahzad *et al.*[4] reported the electrical conductivity of $Ti_3C_2T_x$ films can reach 4600 S cm^{-1}. Therefore, the high aspect ratio of 2D $Ti_3C_2T_x$ flakes can form a conducting network easily within the NiZn ferrite and provide an electron carrier to improve the electrical conductivity of $Ti_3C_2T_x/Ni_{0.5}Zn_{0.5}Fe_2O_4$ composites. In addition, the conductive network formed by 2D $Ti_3C_2T_x$ can be seen as a minicapacitor in the composite. The polarization effects improved the charge storage capacity and the real part of permittivity of the composite. An increase in the imaginary part of the permittivity can be attributed to the increasing ohmic loss in the composite. It is worthy to note that, according to the quarter-wavelength equation, the increases in complex permittivity at high frequency will benefit to decline the absorbing thickness.[5]

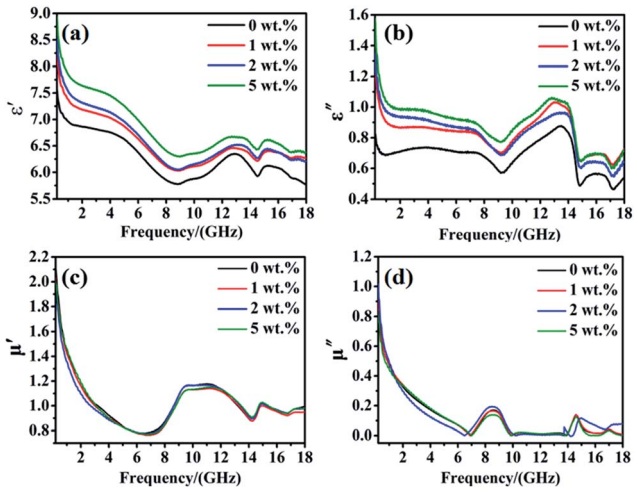

Fig. 9 Complex permittivity (ε_r) and permeability (μ_r) of $Ti_3C_2T_x/Ni_{0.5}Zn_{0.5}Fe_2O_4$ composites with different $Ti_3C_2T_x$ contents: (a) real part of permittivity (ε'); (b) imaginary part of permittivity (ε''); (c) real part of permeability (μ'); and (d) imaginary part of permeability (μ'').

Furthermore, both ε' and ε'' of all specimens exhibits a certain degree of fluctuation in the frequency range of 0.2–18 GHz. The values of both ε' and ε'' first decreased from 0.2–9 GHz and then increased from 9–18 GHz with some obvious resonances. It exhibits obvious frequency-dependent dielectric response. The phenomenon of the values of both ε' and ε'' decreased from 0.2–9 GHz is a typical frequency dispersion behavior, which is common in most of carbon/magnetic composites.[5,15] This may arise from the lag of the induced charges to follow the reversing external field at high frequencies and finally causes a reduction in the electronic oscillations.[38] Furthermore, the permittivity of the $Ti_3C_2T_x/Ni_{0.5}Zn_{0.5}Fe_2O_4$ composites showed typical nonlinear resonant characteristics at 9–18 GHz, which indicates the existence of polarization and relaxation behavior and implies better dielectric loss performance in the corresponding frequency range. Usually, the dielectric property of the material is determined by the electronic, ionic, space charge, Debye dipole and interfacial polarization. As we know, the electronic and ionic polarization is the main contribution in the THz and PHz frequency range. Therefore, the dielectric properties of the $Ti_3C_2T_x/Ni_{0.5}Zn_{0.5}Fe_2O_4$ composites are mainly contributed to space charge, Debye dipole and interfacial polarization. Liu *et al.*[5] observed the similar phenomenon in the co-doped Ni–Zn ferrite/graphene (CNZF/GN) composites. Because of the dielectric properties of $Ti_3C_2T_x/Ni_{0.5}Zn_{0.5}Fe_2O_4$ composites are similar with the CNZF/GN composites. According to the conclusion of Liu *et al.*,[5] the Debye dipolar relaxation effect may be ascribed to the following reason: during the alternation EM wave radiation, the lags in induced charge caused by the ferrite–ferrite, ferrite–$Ti_3C_2T_x$, and $Ti_3C_2T_x$–$Ti_3C_2T_x$ interfaces that encounter the external applied field will lead to relaxation and transformation of EM energy into thermal energy. Furthermore, the lattice defects and functional groups produced from $Ti_3C_2T_x$ and

$Ti_3C_2T_x/Ni_{0.5}Zn_{0.5}Fe_2O_4$ composites synthesis processing would produce additional carries between ferrite and $Ti_3C_2T_x$ and is also beneficial for Debye relaxation. In addition, in the $Ti_3C_2T_x$–$Ni_{0.5}Zn_{0.5}Fe_2O_4$ heterogeneous system, the accumulation of virtual charges at the interface of $Ti_3C_2T_x$ and $Ni_{0.5}Zn_{0.5}Fe_2O_4$ with different conductivities and dielectric constants would lead to interfacial polarization and is well known as Maxwell–Wagner polarization.

In contrast to the permittivity, the incorporation of small fraction of nonmagnetic $Ti_3C_2T_x$ had little effect on the permeability of the $Ti_3C_2T_x/Ni_{0.5}Zn_{0.5}Fe_2O_4$ composites (Fig. 9c and d). The real (μ') and imaginary (μ'') part of the permeability of the all specimens exhibit similar variation trends in the whole frequency range. The values of μ' and μ'' are decreased with an increase in the frequency from 0.2–7 GHz and then some distinct resonance peak could be observed owing to the multiple magnetic resonances. The values of μ' and μ'' are less than 2.1 and 1.1, respectively. Because of the desirable magnetization values, the high initial points (>2) of the real parts of the permeability may be favorable for maintaining a large μ' value and the impedance matching properties in the whole frequency range. The magnetic loss is normally characterized by the imaginary part of permeability (μ''). The imaginary part of permeability shows a decreasing tendency with increasing frequency, which belongs to typical ferromagnetic behavior. In some frequency ranges, the value of imaginary part of the permeability was negative, which indicates that the magnetic energy radiated from these samples owing to the motion of charges in an electromagnetic field.[5] Generally speaking, the magnetic loss of magnetic materials is mainly determined by the domain wall resonance, exchange resonance, hysteresis loss, eddy current resonance, dimensional resonance and natural resonance.[39] The magnetic loss may not be ascribed from the domain wall resonance, because it usually occurs in the megahertz frequency range. Furthermore, for NiZn spinel ferrites, exchange resonance is not the main mechanism of magnetic loss in the high frequency range.[40] In saddition, for the $Ti_3C_2T_x/Ni_{0.5}Zn_{0.5}Fe_2O_4$ composites, the hysteresis loss is proportional to the area of the hysteresis loop. Therefore it can be negligible in a weak field.[41] Moreover, Liu *et al.*[5] calculated the eddy current coefficient and minimum dimensional resonance thickness of the CNZF/GN composites and suggested the absence of an eddy current effect on the magnetic loss. In the present work, the thickness of specimens is about 2 mm, which is smaller than the calculated dimensional resonance thickness (3–4 mm) from wave equations. Therefore, the dimensional resonance can be ignored in the $Ti_3C_2T_x/Ni_{0.5}Zn_{0.5}Fe_2O_4$ composites. Liu *et al.*[5] suggested that the resonance peak in the high frequency range (GHz) should be attributed to natural resonance. Based on these discussion and previous conclusion,[5,39–41] the main mechanism of magnetic loss can be attributed to the natural resonance.

Based on an analysis of the relative complex permittivity and permeability, the EM wave absorption properties of the $Ti_3C_2T_x/Ni_{0.5}Zn_{0.5}Fe_2O_4$ composites were investigated and calculated from the eqn (1) and (2). To further investigate the influence of thickness and frequency on the microwave absorption properties, 3D images map of the reflection loss for various $Ti_3C_2T_x$ contents are shown in Fig. 10a–d. For convenience comparing, the theoretical calculated reflectance of 5 wt% $Ti_3C_2/Ni_{0.5}Zn_{0.5}Fe_2O_4$ with different thicknesses in the frequency range of 0.2–18 GHz was selected to show in Fig. 10e. The peak shows the minimum RL, and the thickness is $n\lambda/4$ (where $n = 1, 3, 5\ldots$). By adjusting the thickness of the specimens from 4 mm to 8 mm, the effective absorption was obtained in the frequency range, 3–7 GHz and 10–15 GHz, respectively. When the thickness was 6.5 mm, the minimum RL value was −42.5 dB at 13.5 GHz. Interestingly, the RL peaks of 5 wt% $Ti_3C_2T_x/Ni_{0.5}Zn_{0.5}Fe_2O_4$ shifted to a lower-frequency with increasing absorber thickness. This phenomenon can be explained by the quarter-wavelength equation:[5]

$$t_m = n\lambda/4 = nc/4f_m(\varepsilon_r/\mu_r)^{1/2} \quad (9)$$

where t_m is the matching thickness at the maximum microwave absorption, f_m is the corresponding frequency, λ is the wavelength of the material, n is an integer ($n = 1, 3, 5\ldots$). From eqn (9), the peak frequency is inversely proportional to the thickness of the absorber. To examine the influence of the $Ti_3C_2T_x$ contents on the absorbing performance of the $Ti_3C_2T_x/Ni_{0.5}Zn_{0.5}Fe_2O_4$ composites, the RL of $Ti_3C_2T_x/Ni_{0.5}Zn_{0.5}Fe_2O_4$ composites with various $Ti_3C_2T_x$ contents were calculated further at a constant thickness of 6.5 mm (Fig. 10f). The minimum reflection loss of the $Ti_3C_2T_x$ content with 0 wt%, 1 wt%, 2 wt%, and 5 wt% was −15.7 dB at 13.5 GHz, −17.4 dB at 13.2 GHz, −18.9 dB at 13.7 GHz, and −42.5 dB at 13.5 GHz, respectively. Two absorption peaks were observed, which indicated that the thickness of the absorber is greater than a critical level of $n = 3$ (eqn (9)). As expected with the experimental design, both the minimum RL value and the effective absorption bandwidth were improved significantly with increasing $Ti_3C_2T_x$ content. This may be due to the increase in permittivity, as shown in Fig. 9. The effective absorption bandwidth of the 5 wt% $Ti_3C_2T_x/Ni_{0.5}Zn_{0.5}Fe_2O_4$ composite reached ~3 GHz (12–15 GHz) in the K-band. It can be observed that, 5 wt% $Ti_3C_2T_x/Ni_{0.5}Zn_{0.5}Fe_2O_4$ composite exhibits superior microwave absorption properties in both the minimum RL value and the effective absorption bandwidth in compare with the other samples. The results indicate that the remarkable effect of $Ti_3C_2T_x$ incorporation on EM wave absorption.

The good microwave absorption performance of $Ti_3C_2T_x/Ni_{0.5}Zn_{0.5}Fe_2O_4$ composites may be explained as follows (Fig. 11):

(1) First, electromagnetic impedance matching plays a key role in the microwave absorption performance of composites. The microwave absorption of pure $Ni_{0.5}Zn_{0.5}Fe_2O_4$ can be attributed mainly to magnetic loss. The imaginary part of complex permittivity is very small at high frequency. Therefore, impedance matching is out of balance. The incorporation of high conductive $Ti_3C_2T_x$ enhanced the conductivity and improved the impedance matching of the $Ti_3C_2T_x/Ni_{0.5}Zn_{0.5}Fe_2O_4$ composites. Therefore, the microwave absorption performance was also improved.

(2) Second, the dielectric loss and magnetic loss are important factors that contribute to EM wave absorption for the

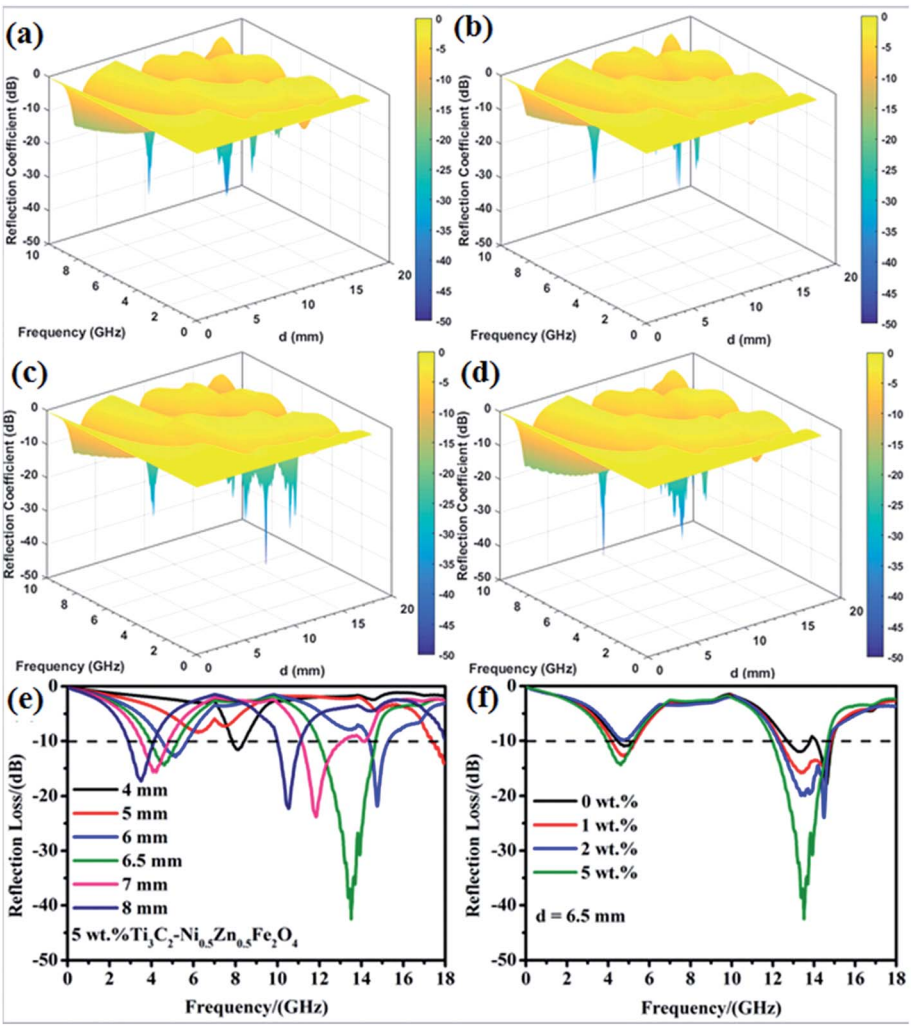

Fig. 10 Three-dimensional representation of the values of reflection los for various $Ti_3C_2T_x$ contents: (a) 0 wt%, (b) 1 wt%, (c) 2 wt%, (d) 5 wt%, (e) reflection loss of a 5 wt% $Ti_3C_2T_x/Ni_{0.5}Zn_{0.5}Fe_2O_4$/paraffin mixture with different thicknesses; (f) reflection loss of the $Ti_3C_2T_x/Ni_{0.5}Zn_{0.5}Fe_2O_4$/paraffin mixture with different $Ti_3C_2T_x$ contents at a thickness of 6.5 mm.

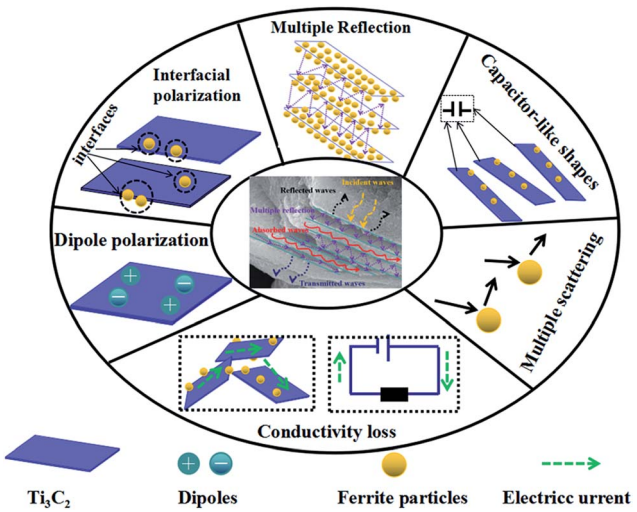

Fig. 11 Schematic diagram of the potential electromagnetic wave absorption mechanisms for the $Ti_3C_2T_x/Ni_{0.5}Zn_{0.5}Fe_2O_4$ composites.

$Ti_3C_2T_x/Ni_{0.5}Zn_{0.5}Fe_2O_4$ composites. The magnetic loss was attributed to the $Ni_{0.5}Zn_{0.5}Fe_2O_4$. As suggested by Han *et al.*[24] and Shahzad *et al.*,[4] the dipolar polarization caused by the surface functional groups, localized defects, and dangling bonds of $Ti_3C_2T_x$ MXenes plays an important role in the dielectric loss. In addition, it is a heterogeneous system. Interfacial polarization, called Maxwel–Wagner polarization, will be generated at the interface of $Ni_{0.5}Zn_{0.5}Fe_2O_4$ and $Ti_3C_2T_x$ MXenes due to the different conductivity and dielectric constants. The *in situ* co-precipitation method used made the nano $Ni_{0.5}Zn_{0.5}Fe_2O_4$ coat the $Ti_3C_2T_x$ MXenes surfaces and inserted interlayer, which can produce a much larger interface of $Ni_{0.5}Zn_{0.5}Fe_2O_4$–$Ti_3C_2T_x$, $Ti_3C_2T_x$–$Ti_3C_2T_x$, and $Ni_{0.5}Zn_{0.5}Fe_2O_4$–$Ni_{0.5}Zn_{0.5}Fe_2O_4$. This can cause strong interface polarization. Under an electromagnetic field, dipolar polarization and interface polarization can increase the energy dissipation, which gives the $Ti_3C_2T_x/Ni_{0.5}Zn_{0.5}Fe_2O_4$ composites enhanced microwave absorption ability.

(3) Third, as demonstrated in the graphene/ferrite composites system, the conductivity loss cannot be ignored because of

the similar excellent conductivity of $Ti_3C_2T_x$ MXenes with graphene.[5] The conductivity network will be formed by the random 2D $Ti_3C_2T_x$ flakes in the $Ti_3C_2T_x/Ni_{0.5}Zn_{0.5}Fe_2O_4$ composites. When the vertical component of an electromagnetic wave is inputted into the composites in an alternating EM field, the EM wave energy is transferred in the form of a micro current due to the good impedance matching.[5] The NiZn ferrites act as an insulator. During micro current transmission, a large portion of the electrical energy would be dissipated due to the high resistance of NiZn ferrites. Moreover a small part is attenuated by $Ti_3C_2T_x$ MXenes itself because the micro current is transmitted to the insulator of NiZn ferrites.

(4) Multiple reflections could be another important absorption mechanism because of the layer structure of $Ti_3C_2T_x$ MXenes, as indicated by Shahzad *et al.*[4] and Han *et al.*[23] Some of the incident EM waves entering the $Ti_3C_2T_x/Ni_{0.5}Zn_{0.5}Fe_2O_4$ composites could be reflected immediately because of the high conductivity of $Ti_3C_2T_x$ MXenes. The remaining waves pass through the MXene and ferrite, where the interaction with the MXenes and ferrite induces a microcurrent that contributes to conductivity losses, resulting in a decrease in the energy of the EM waves. The surviving EM waves will be entered as the next layer of $Ti_3C_2T_x$ and could be reflected and scattered repeatedly between these interfaces. The first and second layers of $Ti_3C_2T_x$ act as the reflecting surface and are enhanced to multiple internal reflections with each other. Furthermore, the NiZn ferrite coated with each $Ti_3C_2T_x$ surface will attenuate the EM waves by magnetic loss and multiple scattering. Therefore, it is difficult for the EM waves to escape from the composites until they are dissipated completely as heat.[17]

4. Conclusion

A facile, fast, and scalable approach to synthesize a novel family $Ti_3C_2T_x$/ferrite composite with good electromagnetic wave absorption was developed using an *in situ* co-precipitation method. The potential electromagnetic wave absorption mechanisms were proposed. The incorporation of high conductivity $Ti_3C_2T_x$ MXenes improved the EM impedance of NiZn ferrite, and contributed to the dielectric loss and conductivity loss of the composites. In addition, the multiple reflections caused by the layer structure of $Ti_3C_2T_x$ MXenes further improved the EM wave absorption performance. The minimum RL value of −42.5 dB at 13.5 GHz with a thickness of 6.5 mm with the 5 wt% $Ti_3C_2T_x$ was obtained. The effective absorption bandwidth of 5 wt% $Ti_3C_2T_x/Ni_{0.5}Zn_{0.5}Fe_2O_4$ composite reached ~3 GHz (12–15 GHz) in the K-band. Although the corresponding thickness of the minimum RL value was relative high, in future work, it is expected to decrease with increasing $Ti_3C_2T_x$ MXenes content. This study is expected to open the door for the potential applications of MXenes/ferrite family in the microwave absorbing field.

Acknowledgements

This study was supported by the National Natural Science Foundation of China (Grant No. 51502310), the Natural Science Foundation of Zhejiang Province (Grant No. LY15E020007), and the Natural Science Foundation of Ningbo city (Grant No. 2016A610248). This study was supported by the National Key Research and Development Program of China (No. 2016YFB0700901).

References

1 B. Zhao, W. Zhao, G. Shao, B. Fan and R. Zhang, *ACS Appl. Mater. Interfaces*, 2015, **7**, 12951–12960.
2 J. Ling, W. Zhai, W. Feng, B. Shen, J. Zhang and W. G. Zheng, *ACS Appl. Mater. Interfaces*, 2013, **5**, 2677–2684.
3 S. Umrao, T. K. Gupta, S. Kumar, V. K. Singh, M. K. Sultania, J. H. Jung, *et al.*, *ACS Appl. Mater. Interfaces*, 2015, **7**, 19831–19842.
4 F. Shahzad, M. Alhabeb, C. B. Hatter, B. Anasori, H. S. Man, C. M. Koo, *et al.*, *Science*, 2016, **353**, 1137–1140.
5 P. Liu, Z. Yao, J. Zhou, Z. Yang and L. B. Kong, *J. Mater. Chem. C*, 2016, **4**, 9738–9749.
6 B. Zhao, B. Fan, S. Gang, W. Zhao and Z. Rui, *ACS Appl. Mater. Interfaces*, 2015, **7**, 18815–18823.
7 Y. Du, W. Liu, R. Qiang, Y. Wang, X. Han, J. Ma, *et al.*, *ACS Appl. Mater. Interfaces*, 2014, **6**, 12997–13006.
8 X. Huang, J. Zhang, M. Lai and T. Sang, *J. Alloys Compd.*, 2015, **627**, 367–373.
9 P. Liu, Z. Yao and J. Zhou, *Ceram. Int.*, 2015, **41**, 13409–13416.
10 V. Sunny, P. Kurian, P. Mohanan, *et al.*, *J. Alloys Compd.*, 2010, **1**, 297–303.
11 Q. Li, Y. Li, X. Li, S. Chen, S. Zhang, J. Wang, *et al.*, *J. Alloys Compd.*, 2014, **608**, 35–43.
12 Y. Li, R. Yi, A. Yan, L. Deng, K. Zhou and X. Liu, *Solid State Sci.*, 2009, **11**, 1319–1324.
13 Y. Wang, Y. Huang, Q. Wang and M. Zong, *Powder Technol.*, 2013, **249**, 304–308.
14 X. Zhou, L. Shen, L. Li, S. Zhou, T. Huang, C. Hu, *et al.*, *J. Eur. Ceram. Soc.*, 2013, **33**, 2119–2126.
15 X. B. Zhou, L. Shen, L. Li, T. M. Huang, C. F. Hu, W. M. Pan, *et al.*, *J. Phys. D: Appl. Phys.*, 2013, **46**, 145002.
16 X. Li, W. Cai, J. An, S. Kim, J. Nah, D. Yang, *et al.*, *Science*, 2009, **324**, 1312–1314.
17 N. Ks, G. Ak, M. Sv, Y. Z. Dj, D. Sv, *et al.*, *Science*, 2004, **306**, 666–669.
18 B. Shen, W. Zhai, M. Tao, J. Ling and W. Zheng, *ACS Appl. Mater. Interfaces*, 2013, **5**, 11383–11391.
19 M. Naguib, M. Kurtoglu, V. Presser, J. Lu, J. Niu, M. Heon, *et al.*, *Adv. Mater.*, 2011, **23**, 4248–4253.
20 M. Naguib, O. Mashtalir, J. Carle, V. Presser, J. Lu, L. Hultman, *et al.*, *ACS Nano*, 2012, **6**, 1322–1331.
21 M. Ghidiu, M. R. Lukatskaya, M. Q. Zhao, Y. Gogotsi and M. W. Barsoum, *Nature*, 2014, **516**, 78–81.
22 M. R. Lukatskaya, O. Mashtalir, C. E. Ren, Y. Dall'Agnese, P. Rozier, P. L. Taberna, *et al.*, *Science*, 2013, **341**, 1502–1505.
23 Z. Ling, C. E. Ren, M. Q. Zhao, J. Yang, J. M. Giammarco, J. Qiu, *et al.*, *Proc. Natl. Acad. Sci. U. S. A.*, 2014, **111**, 16676–16681.
24 M. Han, X. Yin, H. Wu, Z. Hou, C. Song, X. Li, *et al.*, *ACS Appl. Mater. Interfaces*, 2016, **8**, 21011–21019.

25 Y. Qing, W. Zhou, F. Luo and D. Zhu, *Ceram. Int.*, 2016, **42**, 16412–16416.
26 X. Zhou, J. Dai and J. Cai, *J. Chin. Ceram. Soc.*, 2009, **37**, 23–28.
27 S. Brunauer, P. H. Emmett and E. Teller, *J. Am. Chem. Soc.*, 1938, **60**, 309–319.
28 X. Li, G. Fan and C. Zeng, *Int. J. Hydrogen Energy*, 2014, **39**, 14927–14934.
29 X. Li, C. Zeng and G. Fan, *Int. J. Hydrogen Energy*, 2015, **40**, 9217–9224.
30 Q. Peng, J. Guo, Q. Zhang, J. Xiang, B. Liu, A. Zhou, *et al.*, *J. Am. Chem. Soc.*, 2014, **136**, 4113–4116.
31 Y. Tang, J. F. Zhu, C. H. Yang and F. Wang, *J. Alloys Compd.*, 2016, **685**, 194–201.
32 Y. Xiang, W. Xu, Y. Zhan, X. Xia, Y. Xiong, Y. Xiong, *et al.*, *Polym. Compos.*, 2013, **34**, 860–866.
33 X. Li and G. Wang, *J. Magn. Magn. Mater.*, 2009, **321**, 1276–1279.
34 M. Han, X. Yin, L. Kong, M. Li, W. Duan, L. Zhang, *et al.*, *J. Mater. Chem. A*, 2014, **2**, 16403–16409.
35 R. H. Kodama, A. E. Berkowitz, E. J. McNiff Jr and S. Foner, *Phys. Rev. Lett.*, 1996, **77**, 394–397.
36 D. Moitra, M. Chandel, B. K. Ghosh, R. K. Jani, M. K. Patra, S. R. Vadera, *et al.*, *RSC Adv.*, 2016, **6**, 14090–14096.
37 C. Wang, X. J. Han, P. Xu, X. L. Zhang, Y. C. Du, S. R. Hu, *et al.*, *Appl. Phys. Lett.*, 2011, **98**, 217.
38 V. Panwar and R. M. Mehra, *Polym. Eng. Sci.*, 2008, **48**, 2178–2187.
39 B. Lu, X. L. Dong, H. Huang, *et al.*, *J. Magn. Magn. Mater.*, 2008, **6**, 1106–1111.
40 H. Lv, H. Zhang, B. Zhang, *et al.*, *ACS Appl. Mater. Interfaces*, 2016, **8**, 6529–6538.
41 P. Liu, Z. Yao, J. Zhou, *et al.*, *Ceram. Int.*, 2015, **41**, 13409–13416.